




REPORT

# Structural and biochemical insights into lipid transport by VPS13 proteins

Jyoti Adlakha<sup>1,2\*</sup>, , Zhouping Hong<sup>1,2\*</sup>, , PeiQi Li<sup>1</sup>, and Karin M. Reinisch<sup>1,2</sup> 

**VPS13 proteins are proposed to function at contact sites between organelles as bridges for lipids to move directionally and in bulk between organellar membranes. VPS13s are anchored between membranes via interactions with receptors, including both peripheral and integral membrane proteins. Here we present the crystal structure of VPS13s adaptor binding domain (VAB) complexed with a Pro-X-Pro peptide recognition motif present in one such receptor, the integral membrane protein Mcp1p, and show biochemically that other Pro-X-Pro motifs bind the VAB in the same site. We further demonstrate that Mcp1p and another integral membrane protein that interacts directly with human VPS13A, XK, are scramblases. This finding supports an emerging paradigm of a partnership between bulk lipid transport proteins and scramblases. Scramblases can re-equilibrate lipids between membrane leaflets as lipids are removed from or inserted into the cytosolic leaflet of donor and acceptor organelles, respectively, in the course of protein-mediated transport.**

## Introduction

VPS13 family proteins are thought to mediate directional bulk glycerolipid transfer between organelles at contact sites, where organelles are closely apposed, effecting membrane expansion and organelle biogenesis. These proteins feature a single extensive  $\beta$ -sheet that is highly curved to form a taco shell-like structure whose concave surface is lined entirely with hydrophobic residues. The taco shell is long enough to span the cytosolic space between organelles, and the hydrophobic groove along its length can solubilize tens of lipid fatty acid moieties. Recent and ongoing studies are identifying elements at both ends of the proteins that interact with organellar membranes either directly or via adaptor proteins to position the taco shell as a bridge between organelles, allowing lipids to travel between membranes along the hydrophobic groove (reviewed in Dziurdzik and Conibear, 2021; Leonzino et al., 2021). So far the best-characterized members of the family are VPS13 itself, including a single homolog in fungi and four in humans (A–D), and ATG2, whose lipid transfer function is required for autophagosome biogenesis. The human VPS13 proteins are of significant biomedical interest because their dysfunction is linked to severe neurological diseases, including Parkinson’s (VPS13C; Lesage et al., 2016) and chorea acanthocytosis (VPS13A; Rampoldi et al., 2001; Ueno et al., 2001). Among the VPS13 proteins, *Saccharomyces cerevisiae* Vps13p has been the most thoroughly studied and has served as a model system to understand VPS13 function in humans (Dziurdzik et al., 2020; Park et al., 2021).

A major question for VPS13 family proteins is how they localize to and associate with organellar membranes to allow for efficient lipid transfer between the transfer protein and membranes. In yeast, Vps13p localizes to multiple contact sites in part via the so-called VPS13 adaptor binding domain (VAB), near the C-terminal end (Fig. 1 A; Bean et al., 2018). The VAB, with no significant sequence similarity to any previously characterized protein domain, interacts with a Proline-X-Proline (Pro-X-Pro) motif present in receptor proteins at contact sites (Bean et al., 2018). Receptor proteins include the sorting nexin Ypt35p on the endosome, Spo71p on the prospore membrane, and a multipass integral membrane protein, Mcp1p, in the outer mitochondrial membrane (Bean et al., 2018; John Peter et al., 2017). The VAB is present in all VPS13s (but not other VPS13 family proteins like ATG2), including human VPS13 A–D, and likely plays a similar role in their localization, although its human interactome is still unknown and may feature different recognition motifs other than Pro-X-Pro. Here we present the crystal structure, at 3.0-Å resolution, of the VAB from the fungus *Chaetomium thermophilum*, complexed to the Pro-X-Pro motif of Mcp1p from the same organism. We also present biochemical confirmation that the Pro-X-Pro-motifs from Ypt35p and Spo71p bind at the same site as the Mcp1p Pro-X-Pro motif, in agreement with competition studies (Bean et al., 2018).

Parallel studies with the VPS13 family protein ATG2 indicated that ATG2 localizes to contact sites between the ER, where most lipids are synthesized, and nascent autophagosomes, and that

<sup>1</sup>Department of Cell Biology, Yale School of Medicine, New Haven, CT; <sup>2</sup>Aligning Science Across Parkinson’s Collaborative Research Network, Chevy Chase, MD.

\*J. Adlakha and Z. Hong contributed equally to this paper. Correspondence to Karin M. Reinisch: [karin.reinisch@yale.edu](mailto:karin.reinisch@yale.edu).

© 2022 Adlakha et al. This article is available under a Creative Commons License (Attribution 4.0 International, as described at <https://creativecommons.org/licenses/by/4.0/>).

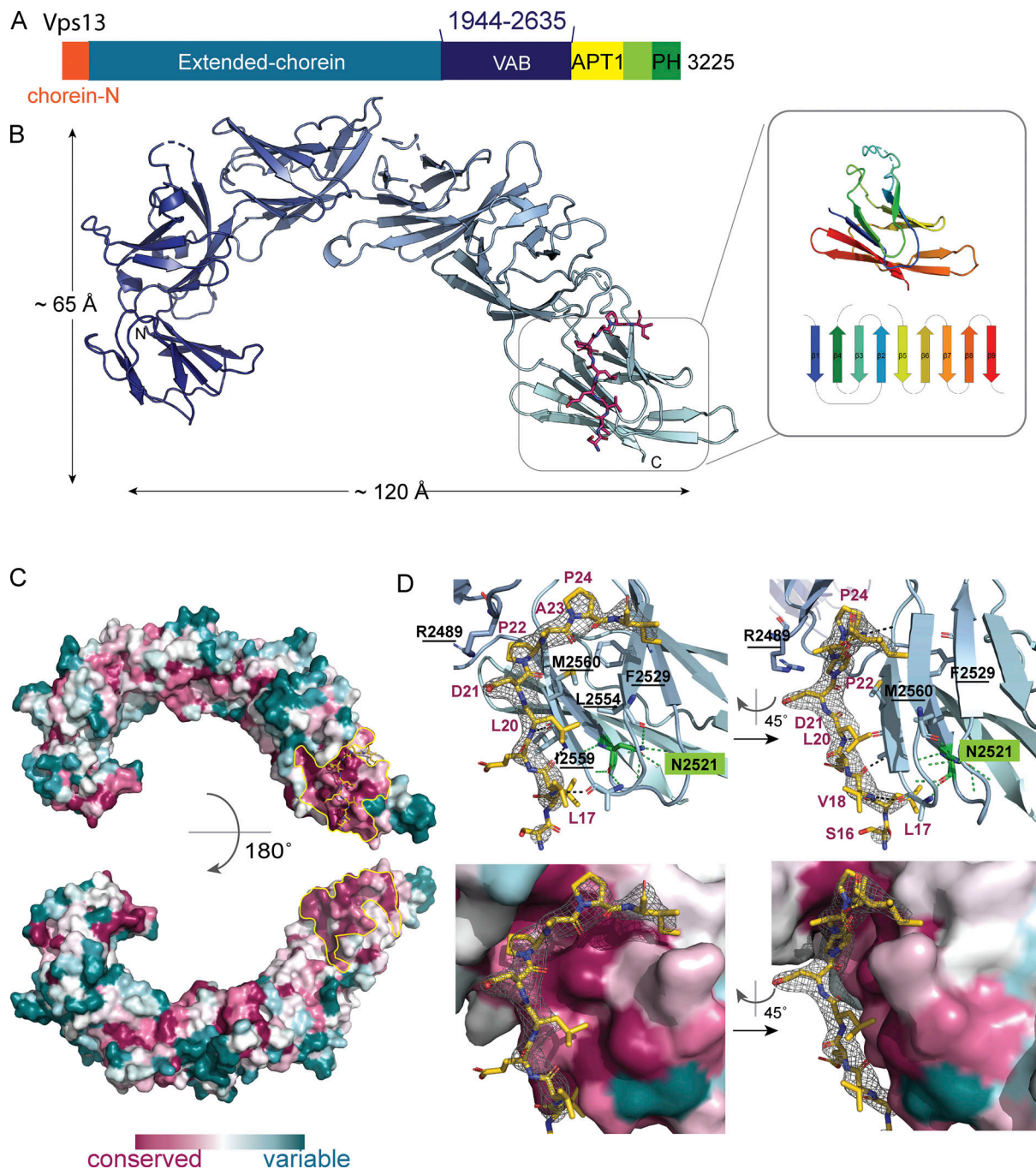


**Figure 1. Architecture of the VAB and its Pro-X-Pro motif binding site.** (A) Schematic showing domain architecture of Vps13p. Residue numbers refer to the *C. thermophilum* Vps13p sequence. (B) Ribbons diagram for the VAB from *C. thermophilum*, showing its six repeated modules. The Pro-X-Pro motif is colored magenta. Inset shows one module, colored from blue at the N-terminus to red at the C-terminus, and a topology diagram colored in the same way. Fig. S1 A shows differences between the crystal structure and the AlphaFold2 prediction. (C) Sequence conservation, based on an alignment of 1,000 fungal Vps13s as determined by Consurf (Ashkenazy et al., 2016) and mapped onto the VAB surface. A patch centered on the sixth repeat and including the interface between the fifth and sixth repeats, outlined in yellow, is highly conserved and is the binding site for the receptor Pro-X-Pro motif. For electrostatic potential mapping, see Fig. S1 B. (D) Difference density from a 2Fo-Fc map (3.0 I/σ contour level), into which the Pro-X-Pro binding motif was modeled, is shown. Top: Two views of the Pro-X-Pro binding motif (yellow) bound to the VAB (light blue). Residues in the VAB binding surface, including those that were mutated to abrogate binding of the Pro-X-Pro motif, are labeled (mutated residues underlined). The asparagine in the sixth module at the end of β1, which is conserved in all modules, and which was mutated in previous interaction studies (Dziurdzik et al., 2020), is labeled (N2521). In the protein interior, it is part of an extensive hydrogen bonding network that stabilizes module folding (Fig. S1 C).

ATG2 interacts with scramblases both in the ER and in the autophagosome (Ghanbarpour et al., 2021; Maeda et al., 2020; Matoba et al., 2020). We and others proposed previously that the scramblases allow for directional bulk lipid flow by restoring the bilayer symmetry of both the donor and acceptor membranes as lipids are asymmetrically removed from or inserted into their cytosolic leaflet in the course of protein-mediated lipid transfer. Here we present evidence that the VPS13s themselves also work with lipid scramblases, showing scramblase activity for both Mcp1p, the Pro-X-Pro motif containing protein that interacts with yeast Vps13p at mitochondria (Bean et al., 2018; John Peter et al., 2017), and XK (also known as XKR1), which interacts with VPS13A in humans (Park and Neiman, 2020). XK-related protein-4, -8, and -9 are known caspase-activated scramblases in the plasma membrane (Suzuki et al., 2014), but no such activity has been previously reported for XK itself. Our data support a model in which bulk lipid transporters in the VPS13 family function in collaboration with scramblases.

## Results and discussion

To better understand how VPS13s might interact with organellar membranes, we undertook a structural characterization of the VAB. Although we were unsuccessful in crystallizing the VAB domain by itself, we did obtain crystals of a construct comprising the VAB of *C. thermophilum* Vps13p (residues 1,944–2,635) N-terminally fused to the Pro-X-Pro-motif of Mcp1 (residues 15–32), PXP(Mcp1<sub>ct</sub>)-VAB<sub>ct</sub>. The crystals belong to spacegroup P2<sub>1</sub> and diffract to 3.0 Å. We used molecular replacement for phasing with a model for the VAB derived from AlphaFold2 (Jumper et al., 2021). The VAB comprises six modules of the same topology arranged end to end to resemble a fishhook (Fig. 1 B). Each module features nine β-strands connected by loops and arranged into a β-sandwich, similar to that of lysins such as osteolysin (Protein Data Bank [PDB] accession no. 6MYI) or hemolysin (PDB accession no. 6ZC1; Fig. 1 B, inset). There are two VAB molecules in each asymmetric unit. We were able to model all six of the modules in one copy, PXP-VAB<sub>1–6</sub>. In the second copy, PXP-VAB<sub>1–5</sub>, we modeled only the first five repeated modules (residues 1,944–2,516), as the electron density for the sixth repeat was poor, most likely because this repeat is flexibly positioned with respect to the rest of the protein. The first five modules for the two copies of the VAB in the crystal superimpose closely (root-mean-square deviation over 428 Ca's is 0.48 Å). (A comparison of PXP-VAB<sub>1–6</sub> and the AlphaFold2 prediction is shown in Fig. S1 A; major differences exist at the interfaces between repeated modules.) One face of *C. thermophilum* VAB is largely acidic, whereas the other has a large basic patch (Fig. S1 B). A prominent patch on the surface of the sixth module and extending to the interface between the fifth and sixth modules is highly conserved across fungi, indicating functional importance (Fig. 1 C). Indeed, this surface includes the binding site for the Pro-X-Pro motif (below). A similar surface, on the sixth repeat and at its interface with the fifth repeat, is highly conserved in comparisons of metazoan VPS13 VABs as well, indicating a key function, likely also in receptor binding. The patch residues, however, are less well

conserved in comparing fungal and metazoan VABs, possibly because the metazoan VPS13s recognize different receptor motifs, other than Pro-X-Pro.

There is strong density for the Pro-X-Pro-motif fused to the N-terminus of PXP-VAB<sub>1–5</sub> (L<sub>17</sub>V<sub>18</sub>E<sub>19</sub>L<sub>20</sub>D<sub>21</sub>P<sub>22</sub>A<sub>23</sub>P<sub>24</sub>I<sub>25</sub>A<sub>26</sub>E<sub>27</sub>), showing that it interacts in trans with PXP-VAB<sub>1–6</sub>, binding on the acidic face of the VAB at the conserved interface between its fifth and sixth repeats (Fig. 1 D). Residues L17–D21 form a short β-strand alongside and parallel to the fourth β-strand of the sixth repeat module, with the two conserved hydrophobic residues (L17 and L20) packed against hydrophobic surfaces. The two proline side chains (P22 and P24) are buried in a groove that runs along the interface. The strong conservation of residues forming the Pro-X-Pro-binding site in PXP-VAB<sub>1–6</sub> support that this binding surface is physiologically relevant and not an artifact of crystallization. The Pro-X-Pro motif at the N-terminus of PXP-VAB<sub>1–6</sub> appears to be disordered, as there is no density for it in the electron density maps. It is likely that, because of crystal packing constraints, the peptide cannot access the binding site in PXP-VAB<sub>1–5</sub>, or the binding site is not formed in PXP-VAB<sub>1–5</sub> (the sixth module is not visible in the density), or both.

A Pro-X-Pro binding site at the interface of the fifth and sixth modules of the VAB is consistent with previously reported biochemical experiments, indicating that the fifth and sixth repeat modules are sufficient for binding the Pro-X-Pro motif (Dziurdzik et al., 2020). Further, mutation of an asparagine residue at the C-terminal end of the first β-strand of the sixth repeat module of the VAB (N2521 in *C. thermophilum* Vps13p) abolished Pro-X-Pro binding (Dziurdzik et al., 2020). This asparagine, in the protein interior, does not form part of the Pro-X-Pro motif binding surface of the VAB as observed in the crystal structure (see Fig. 1 E) but is highly conserved in all modules, as part of an extensive hydrogen bonding network stabilizing the module's core (including the β3–β4 hairpin at the Pro-X-Pro peptide binding site; Fig. S1 C). Its mutation to an alanine very likely destabilizes the sixth repeat module, at least locally, preventing formation of the Pro-X-Pro binding site. (Mutation of the corresponding asparagine in the most N-terminal repeat module, which is far removed from the identified Pro-X-Pro binding site, was also reported to abolish VPS13 interactions with its receptor proteins [Dziurdzik et al., 2020]. Possibly this mutation causes local destabilization to perturb packing of the first against the second VAB repeat modules, thus somehow affecting the structure of the VAB or its positioning within the full-length VPS13 to interfere with receptor binding.)

Further characterization of the *C. thermophilum* VAB alone, the PXP(Mcp1<sub>ct</sub>)-VAB<sub>ct</sub> construct used in crystallization, and a construct in which the Pro-X-Pro-motif is C-terminally fused to the VAB, VAB<sub>ct</sub>-PXP(Mcp1<sub>ct</sub>), further supports the proposed binding site between the fifth and sixth modules. Both size exclusion chromatography and negative stain EM indicate that the VAB alone and VAB<sub>ct</sub>-PXP(Mcp1<sub>ct</sub>), where the Pro-X-Pro-motif can access the proposed binding site in cis, are monomeric (Fig. 2, A–D). In contrast, PXP(Mcp1<sub>ct</sub>)-VAB<sub>ct</sub> forms dimers (Fig. 2, A and D). In this case, the N-terminal Pro-X-Pro motif is too far from the binding site to access it in cis and instead



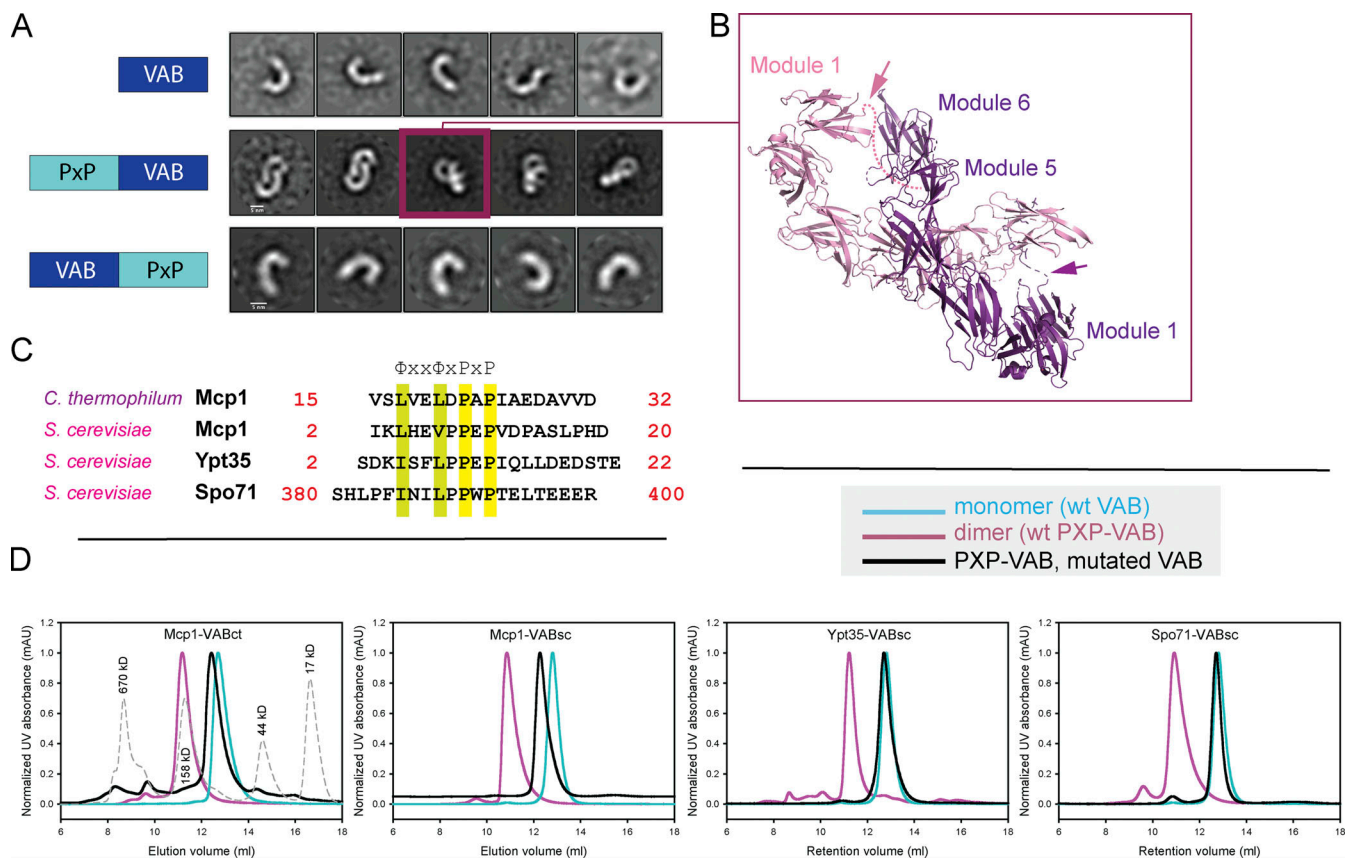


**Figure 2. The Pro-X-Pro motifs of Mcp1p, Spo71p, and Ypt35p bind to the same surface of the VAB.** (A) The VAB<sub>ct</sub> and VAB<sub>ct</sub>-PXP(Mcp1<sub>ct</sub>) constructs are monomeric in solution as assessed by negative stain EM, whereas PXP(Mcp1<sub>ct</sub>)-VAB<sub>ct</sub> dimerizes. Class averages are shown (scale bar, 5 nm). (B) PXP(Mcp1<sub>ct</sub>)-VAB<sub>ct</sub> dimerization is in trans, with the N-terminal PXP-motif from one monomer bound to the C-terminal end of the second monomer and vice versa. The dimer in the asymmetric unit of the crystal is similar to the class average boxed in A. (C) Pro-X-Pro motifs of Mcp1p from *C. thermophilum* and *S. cerevisiae*, and from *S. cerevisiae* Spo71p and Ytp35p. (D) Size-exclusion profiles of wild-type and mutant constructs of PXP(Mcp1<sub>ct</sub>)-VAB<sub>ct</sub>, PXP(Mcp1<sub>sc</sub>)-VAB<sub>sc</sub>, PXP(Spo71<sub>sc</sub>)-VAB<sub>sc</sub>, and PXP(Ytp35<sub>sc</sub>)-VAB<sub>sc</sub>. The wild-type constructs are dimers, indicating an intact Pro-X-Pro binding site. For the mutants, residues important for the binding of the Pro-X-Pro motif as determined from the crystal structure were altered, and the constructs are monomeric. This shows that the Pro-X-Pro motifs of Mcp1p, Spo71p, and Ytp35p all bind this site on the VAB surface. mAU, milli absorbance units.

accesses it in trans (Fig. 2 B). When we introduced mutations to perturb the identified binding site (R2489E, L2554A, I2559A, and M2560A; see Fig. 1 D), PXP(Mcp1<sub>ct</sub>)-VAB<sub>ct</sub> no longer dimerized, indicating that the Pro-X-Pro motif no longer binds (Fig. 2 D).

We used a similar approach to assess whether, as was reported, the Pro-X-Pro motifs of Spo71p and Ypt35p bind in the same site. We made PXP-VAB<sub>sc</sub> constructs in which we N-terminally fused the Pro-X-Pro motifs from *S. cerevisiae* Mcp1p (residues 2–20), Spo71p (residues 380–400), or Ypt35p (residues 2–22; see Fig. 2 C for sequences) to the *S. cerevisiae* VAB (residues 1,869–2,545) or a mutated version, in which the residues in the proposed Pro-X-Pro-binding surface were altered as before (R2396E, I2468A, I2473A, and M2474A). Whereas the PXP-VAB<sub>sc</sub> constructs with the wild-type VAB sequence dimerized, the mutant PXP-VAB<sub>sc</sub> constructs were monomeric, indicating that the Pro-X-Pro motifs of Mcp1p, Spo71p, and Ypt35p all bind in the same site (Fig. 2 D).

To assess the notion that VPS13 proteins act in collaboration with scramblases, like the VPS13 family protein ATG2, we used a well-established fluorescence-based assay to determine whether multispan proteins known to interact directly with VPS13 proteins, Mcp1p (Bean et al., 2018; John Peter et al., 2017) and XK

(Park and Neiman, 2020), might scramble glycerolipids (Goren et al., 2014; Ploier and Menon, 2016). We overexpressed these proteins, purified them in detergent (*n*-dodecyl- $\beta$ -D-maltoside [DDM] and glyco-diosgenin [GDN] for Mcp1p and XK, respectively), and reconstituted them into liposomes containing small (0.5%) amounts of nitrobenzoxadiazole (NBD)-labeled lipid (Fig. 3 A). The addition of dithionite, a membrane-impermeable reducing agent, reduces solvent accessible NBD to quench its fluorescence. In the absence of scramblase activity, dithionite can access NBD only in the outer leaflet of the liposome but not in the liposome lumen, so dithionite addition results in a ~50% reduction in fluorescence (Fig. 3 B). In the presence of a scramblase, which continuously exchanges NBD-lipids between the leaflets of the membrane bilayer, all NBD becomes accessible, resulting in a larger, near-complete (>>50%) reduction in fluorescence upon dithionite addition. The reduction would be complete in an ideal reconstitution scenario, in which all liposomes incorporate scramblase activity.

Using this assay, we found that both Mcp1p and XK scramble glycerolipids nonspecifically, including phosphatidylethanolamine (PE), phosphatidylcholine (PC), and phosphatidylserine

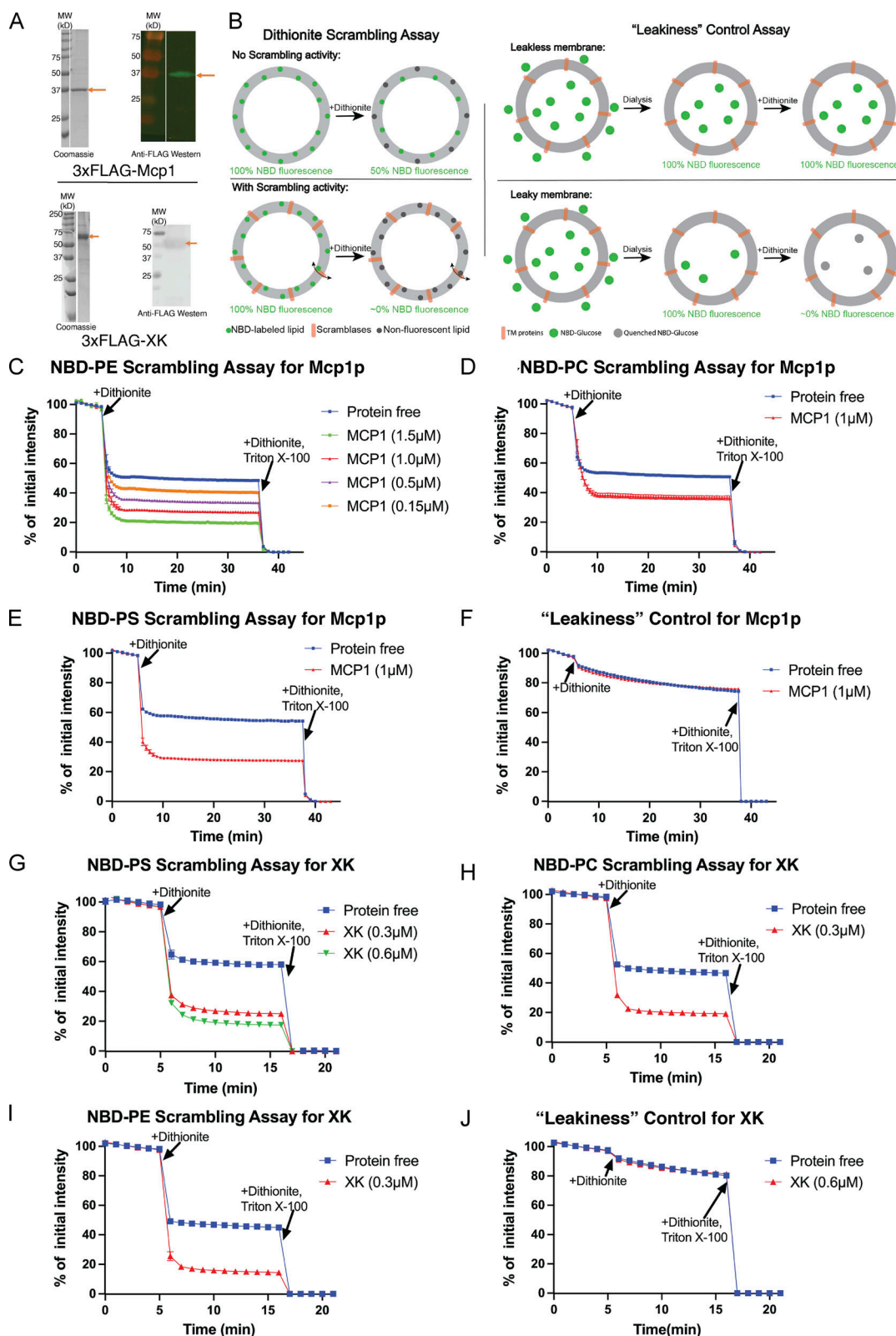


Figure 3. **Mcp1p and XK scramble glycerolipids in vitro.** (A) SDS-PAGE gels showing purified 3xFLAG-Mcp1p or 3xFLAG-XK before their reconstitution into liposomes, analyzed by Coomassie staining and by Western blotting with anti-FLAG. (B) Schematics for the dithionite scrambling assay and leakiness control. TM, transmembrane. (C) Mcp1p scrambles NBD-PE. Scrambling is not observed with the protein-free liposomes. Reconstitution is more efficient when the protein is added at higher concentrations, resulting in nearly complete reduction of fluorescence. (D and E) Mcp1p scrambles NBD-PC and NBD-PS. (F) Leakiness control for Mcp1p-containing liposomes. Fluorescence retention of NBD-glucose in the liposome lumen after dialysis and, further, after addition of dithionite indicates that the liposome membranes remain intact and impermeable to small molecules like dithionite or NBD-glucose. (G–I) Scrambling results for XK. XK scrambles NBD-lipids without headgroup specificity. (J) The XK-containing liposomes are leak-free. Source data are available for this figure: SourceData F3.





We anticipate that additional scramblases will continue being identified as the known VPS13 interactome expands. It is also possible that the VPS13 proteins partner with other multipass integral membrane proteins that do not have scrambling activity. For example, these could be part of the lipid biosynthetic machinery, allowing lipids to be removed from the membrane leaflet in which they are made to another compartment as they are made. Such a scenario was recently proposed for a newly identified member of the VPS13 family, Csflp (Toulmay et al., 2022). We predict that this model of a partnership between scramblases, or other classes of multipass integral membrane proteins, and lipid transporters will also be applicable to more recently identified members of the VPS13 protein family, including SHIP164, KIAA1109/Csflp, and Hobbit/Hob1p/Hob2p (Gomes Castro et al., 2021; Hanna et al., 2021; John Peter et al., 2021; Neuman et al., 2022; Toulmay et al., 2022). Coordinates and structure factors for the VPS13 VAB have been deposited with PDB (accession no. 7U8T).

## Materials and methods

All the lipids including 1-palmitoyl-2-oleoyl-*sn*-glycero-3-phosphocholine (POPC; 850457C), 1-palmitoyl-2-oleoyl-*sn*-glycero-3-phosphoethanolamine (POPE; 850757C), NBD-PE (810153C), NBD-PC (810122), and NBD-PS (810198) were purchased from Avanti Polar Lipids. NBD-glucose was purchased from Abcam (186689-07-6), DDM from GoldBioTech (DDM25), and GDN from Anatrache (GDN101). Bio-Beads SM2 Adsorbent Media was purchased from Bio-Rad (152-3920), anti-FLAG M2 resin from Sigma-Aldrich (A2220), and EDTA-free cOmplete protease inhibitor cocktail from Roche (4693159001). Expi293F cells and *Escherichia coli* BL21 (DE3)-competent cells were purchased from Thermo Fisher Scientific (A14527 and C600003).

## Structural and biochemical studies of the VPS13 VAB

### Plasmid constructs

The VAB domain (residues 1,944–2,635) of Vps13p from *C. thermophilum* (Uniprot GOS388) was cloned from genomic DNA into a modified pET-Duet vector with a C-terminal 6xHis tag. To generate PxP(Mcplct)-VABct<sub>1,944–2,635</sub>-His<sub>6</sub>, residues 15–32 of Mcp1 from *C. thermophilum* (Uniprot GOS0T5) were fused N-terminally to the VAB<sub>1,944–2,635</sub>-His<sub>6</sub> construct. VAB domain (residues 1,869–2,545) of Vps13p from *S. cerevisiae* was similarly cloned from genomic DNA into pET-29a(+) expression vector containing a C-terminal 6xHis tag. PxP(Mcplsc)-VABsc<sub>1,869–2,545</sub>-His<sub>6</sub>, PxP(Ypt35sc)-VABsc<sub>1,869–2,545</sub>-His<sub>6</sub>, and PxP(Spo7lsc)-VABsc<sub>1,869–2,545</sub>-His<sub>6</sub> constructs contain N-terminal fusion of residues 2–20 from yeast Mcp1, residues 2–22 from Ypt35, and residues 380–400 from Spo7l, respectively. All mutants were generated by round-the-horn mutagenesis. See Table S1 for a list of primers.

### Protein expression and purification

All plasmids were transformed in *E. coli* BL21 (DE3) cells. Cells were cultured at 37°C until OD (600 nm) reached 0.8, and protein expression was induced with 0.5 mM IPTG at 18°C for 16 h. Harvested cells were resuspended in buffer A (20 mM Hepes,

pH 7.8, 500 mM NaCl, 1 mM tris(2-carboxyethyl)phosphine [TCEP].HCl, and 10% glycerol) supplemented with 20 mM imidazole, 5 mM MgCl<sub>2</sub>, DnaseI, and 1× cOmplete EDTA-free protease inhibitor cocktail (Roche), lysed using a cell disruptor (5 passes at 15,000 psi), and clarified by centrifugation at 15,000 rpm for 45 min. Cell lysate was loaded on Ni<sup>2+</sup>-NTA column pre-equilibrated with lysis buffer. After washing, bound protein was eluted with buffer A containing 500 mM imidazole, concentrated using an Amicon Ultra centrifugal filter unit with a 50-kD molecular weight cutoff, and loaded on a Superdex 200 gel filtration column (GE Healthcare) equilibrated with buffer A.

Protocols for construct expression and purification are available at <https://dx.doi.org/10.17504/protocols.io.yxmvnmnejog3p.v1>.

### Crystallization, data collection, and structure determination

PxP(Mcplct)-VABct<sub>1,944–2,635</sub>-His<sub>6</sub> was crystallized with sitting-drop vapor diffusion method. Equal volumes of protein at 3 mg/ml concentration and reservoir solution (75 mM imidazole, pH 8.2, 70 mM Li<sub>2</sub>SO<sub>4</sub>, and 500 mM NaCl) were mixed and incubated at 295°K. Plate-like crystals, belonging to space group P2<sub>1</sub>, were cryoprotected by serial transfer in mother liquor containing increasing concentrations of glycerol, loop-mounted, and flash frozen in liquid nitrogen. Diffraction data were collected at 100°K and a wavelength of 0.979 Å at the Northeastern Collaborative Access Team (NE-CAT) beamline 24-ID-E at the Advanced Photon Source, using a Dectris EIGER 16M detector (Dectris). All data were indexed, integrated, and scaled using XDS (Kabsch, 2010), with the statistics given in Table S2. The structure of PxP(Mcplct)-VABct<sub>1,944–2,635</sub>-His<sub>6</sub> was solved by molecular replacement with Phaser MR (McCoy et al., 2007), using a model generated with the AlphaFold2 Colab notebook (Jumper et al., 2021) preprocessed with phenix.process\_predicted\_model (Liebschner et al., 2019) to remove low-confidence residues with pLDDT scores <70. The first three repeat modules were initially searched and confidently placed in the electron density, followed by the next two modules in both chains. Finally, the sixth repeat module was identified for only one of the chains (PxP-VAB<sub>1–6</sub>). After jelly body refinement, strong and continuous density corresponding to the Pro-X-Pro peptide appeared in 2Fo-Fc maps (Fig. 1 D). In modeling the peptide into this density, we were guided by the restraints imposed by the linker length, as the Pro-X-Pro peptide binds in trans, stretching from the N-terminus of one molecule to its binding site on the other. This restraint set the directionality of the peptide chain. A prominent feature of the backbone density was a kink, into which the Pro-Ala-Pro sequence was modeled, with both prolines featuring cis peptide bonds. Maps calculated once these residues and the rest of the peptide's polyaniline backbone had been placed showed good side chain density, allowing us also to model side chains for other residues in the Pro-X-Pro motif. We further checked difference maps to adjust side chain positions during refinement. The peptide register as modeled was the best fit to this density. The refinement consisted of cycles of manual model rebuilding in COOT (Emsley et al., 2010) and individual isotropic B-factor and TLS refinement with REFMAC5 (Murshudov et al., 2011) and phenix.refine (Liebschner et al., 2019). Refinement statistics are given in Table

S2. Structures were rendered in PyMol (PyMOL Molecular Graphics System, v2.0; Schrödinger).

Protocols for crystallization, data collection, and structure determination are available at <https://dx.doi.org/10.17504/protocols.io.dm6gpbz68lp/v1>.

## Scrambling studies for Mcp1p and XK

### Plasmids

The coding sequences of MCP1 (Uniprot Q12106) and XK (Uniprot P51811) were PCR amplified from *S. cerevisiae* genomic DNA and human cDNA libraries, respectively, and subcloned into pCMV10 vector with an N-terminal 3xFLAG tag and PreScission protease cleavage site.

### Membrane protein expression and purification

Constructs encoding MCP1 or XK were transfected into Expi293F cells (Thermo Fisher Scientific) according to the manufacturer's instructions. The cells were harvested 48 h after transfection.

For Mcp1p, the cells were pelleted and resuspended in buffer B (50 mM Hepes, pH 7.0, 500 mM NaCl, 1 mM TCEP, and 10% glycerol) containing 1× cComplete EDTA-free protease inhibitor cocktail (Roche) and lysed using a Dounce homogenizer (15–20 passes). To solubilize the protein, powdered DDM was added to the lysate at a final concentration of 1% wt/vol, and the lysate was gently agitated in the cold room for 90 min. Cell lysates were clarified via centrifugation at 100,000 *g* for 60 min; supernatant was incubated with anti-FLAG M2 resin (Sigma-Aldrich), which was pre-equilibrated with buffer C (buffer B and 0.02% DDM) at 4°C for 2 h; and the resin was washed with buffer C. To remove chaperone, resin was incubated with buffer C containing 5 mM MgCl<sub>2</sub> and 2.5 mM ATP at 4°C overnight. Bound proteins were further washed with buffer C and eluted using 0.25 mg/ml 3xFlag peptide in buffer C. The proteins were concentrated in a 10-kD molecular weight cutoff Amicon centrifugal filtration device (UFC501024) and quantified by Coomassie blue staining using BSA standards.

XK was purified similarly to Mcp1p but with buffer D (50 mM Hepes, pH 7.8, 200 mM NaCl, 1 mM TCEP, and 10% glycerol) and with GDN instead of DDM throughout (1.5% GDN for solubilization and 0.02% GDN for purification). XK was further gel filtrated with Superdex 200 increase 10/300 column (Cytiva).

**Liposome preparation.** 90% POPC, 9.5% POPE, and 0.5% NBD-labeled lipid (NBD-PE, NBD-PC, or NBD-PS) in chloroform were mixed and dried under a N<sub>2</sub> stream and further vacuum dried for 30 min. The resulting lipid film was resuspended in buffer E (50 mM Hepes, pH 7.0, and 200 mM NaCl) for MCP1 and buffer F (50 mM Hepes, pH 8.0, and 200 mM NaCl) for XK to generate a 10.5-mM lipid stock. The mixture was incubated at 37°C for 60 min, with vortexing every 10 min, and then freeze-thawed for 10 cycles. Liposomes were extruded 31 times through a 400-nm polycarbonate filter and used within 6 h.

### Proteoliposome preparation

Proteoliposomes were prepared as described in [Marek and Gunther-Pomorski \(2016\)](#) and [Ploier and Menon \(2016\)](#). Briefly, liposomes at final lipid concentration of 5.25 mM and in 250 µl total volume were destabilized by addition of Triton X-

100 to a final concentration determined by the swelling titration assay as described in [Ploier and Menon \(2016\)](#). The final Triton X-100 concentration was 3 mM. After 2 h of destabilization at room temperature, detergent-solubilized proteins (MCP1 or XK) were added, and the samples were gently agitated for an hour to allow protein incorporation. The detergent was removed in three steps using prewashed Bio-Beads: after a first addition of Bio-Beads (20 mg), the sample was incubated at room temperature for an hour; then another aliquot of Bio-Beads (20 mg) was added, and the sample was rotated at room temperature for two more hours. Finally, the sample was pipetted into a new tube containing fresh Bio-Beads (40 mg) and agitated at 4°C overnight. Bio-Beads were removed by pipetting, and the sample was dialyzed against buffer E for MCP1 and buffer F for XK for 2 d at 4°C. The protein reconstitution efficiency was ~100% as assessed using a liposome flotation assay ([Karatekin and Rothman, 2012](#)).

### Scrambling assay

The scrambling assay ([Goren et al., 2014](#); [Ploier and Menon, 2016](#)) was performed at 30°C in 96-well plates, with 100-µl reaction volumes of liposomes/proteoliposomes (~260 µM final lipid concentration) prepared as described above. To assess scrambling, NBD fluorescence after addition of dithionite (to 5 mM) was monitored (excitation at 460 nm, emission at 538 nm) using the Synergy H1 Hybrid Multi-Mode Reader (BioTek). Finally, additional dithionite (5 mM) and Triton X-100 (0.5%) were added. The Triton X-100 dissolves the liposomes, allowing complete quenching of the NBD.

A similar protocol was used for the NBD-glucose leakiness control assay ([Goren et al., 2014](#); [Ploier and Menon, 2016](#)), except that no NBD-lipids were incorporated into the liposomes or proteoliposomes. Instead, NBD-glucose (3 mM) was added during the destabilization step.

Protocols for the expression and purification of Mcp1p and XK, their reconstitution into liposomes and scrambling assays are available at <https://dx.doi.org/10.17504/protocols.io.kxygxzyqdv8j/v1>.

### Online supplemental material

**Fig. S1** contains details of the VAB structure. Table S1 lists primers for the study. Table S2 lists data collection and refinement statistics.

## Acknowledgments

We thank T. Melia and P. De Camilli for critically reading this manuscript and the staff of NE-CAT beamlines of the Advanced Photon Source (Argonne National Laboratory) for their help with data collection.

NE-CAT is funded by the National Institute of General Medical Sciences of the National Institutes of Health (NIH; P30 GM124165), NIH-ORIP HEI grant (S10OD021527), and contract DE-AC02-06CH11357. This research was funded by grants from the NIH (R35GM131715) and by Aligning Science Across Parkinson's grant ASAP-000580 through the Michael J. Fox Foundation for Parkinson's Research to K.M. Reinisch. Z. Hong was also supported by the China Scholarship Council. For the



purpose of open access, the author has applied a CC-BY public copyright license to the Author Accepted Manuscript (AAM) version arising from this submission.

The authors declare no competing financial interests.

Author contributions: K.M. Reinisch conceived of and supervised experiments. P. Li designed the VAB constructs used in crystallization and obtained initial crystallization conditions. J. Adlakha optimized crystallization and cryo-conditions, determined and analyzed the structure, and carried out all VAB-related biochemistry. Z. Hong made proteins for and carried out all scrambling assays. J. Adlakha and Z. Hong made the figures. K.M. Reinisch wrote the manuscript together with J. Adlakha and Z. Hong.

Submitted: 7 February 2022

Revised: 10 March 2022

Accepted: 14 March 2022

## References

- Ashkenazy, H., S. Abadi, E. Martz, O. Chay, I. Mayrose, T. Pupko, and N. Ben-Tal. 2016. ConSurf 2016: An improved methodology to estimate and visualize evolutionary conservation in macromolecules. *Nucleic Acids Res.* 44:W344–W350. <https://doi.org/10.1093/nar/gkw408>
- Baek, M., F. DiMaio, I. Anishchenko, J. Dauparas, S. Ovchinnikov, G.R. Lee, J. Wang, Q. Cong, L.N. Kinch, R.D. Schaeffer, et al. 2021. Accurate prediction of protein structures and interactions using a three-track neural network. *Science*. 373:871–876. <https://doi.org/10.1126/science.abj8754>
- Bean, B.D.M., S.K. Dziurdzik, K.L. Kolehmainen, C.M.S. Fowler, W.K. Kwong, L.I. Grad, M. Davey, C. Schluter, and E. Conibear. 2018. Competitive organelle-specific adaptors recruit Vps13 to membrane contact sites. *J. Cell Biol.* 217:3593–3607. <https://doi.org/10.1083/jcb.201804111>
- Dziurdzik, S.K., B.D.M. Bean, M. Davey, and E. Conibear. 2020. A VPS13D spastic ataxia mutation disrupts the conserved adaptor-binding site in yeast Vps13. *Hum. Mol. Genet.* 29:635–648. <https://doi.org/10.1093/hmg/ddz318>
- Dziurdzik, S.K., and E. Conibear. 2021. The Vps13 family of lipid transporters and its role at membrane contact sites. *Int. J. Mol. Sci.* 22:2905. <https://doi.org/10.3390/ijms22062905>
- Emsley, P., B. Lohkamp, W.G. Scott, and K. Cowtan. 2010. Features and development of Coot. *Acta Crystallogr. D Biol. Crystallogr.* 66:486–501. <https://doi.org/10.1107/S0907444910007493>
- Fidler, D.R., S.E. Murphy, K. Courts, P. Antonoudiou, R. El-Tohamy, J. Ient, and T.P. Levine. 2016. Using HHsearch to tackle proteins of unknown function: A pilot study with PH domains. *Traffic*. 17:1214–1226. <https://doi.org/10.1111/tra.12432>
- Ghanbarpour, A., D.P. Valverde, T.J. Melia, and K.M. Reinisch. 2021. A model for a partnership of lipid transfer proteins and scramblases in membrane expansion and organelle biogenesis. *Proc. Natl. Acad. Sci. USA*. 118. <https://doi.org/10.1073/pnas.2101562118>
- Gomes Castro, I., S.P. Shortill, S.K. Dziurdzik, A. Cadou, S. Ganesan, E.J. Fenech, H. Meyer, A. Fadel, Y. David, M. Davey, et al. 2021. Systematic analysis of membrane contact sites in *Saccharomyces cerevisiae* uncovers modulators of cellular lipid distribution. *bioRxiv*. <https://doi.org/10.1101/2021.10.17.464712>
- Goren, M.A., T. Morizumi, I. Menon, J.S. Joseph, J.S. Dittman, V. Cherezov, R.C. Stevens, O.P. Ernst, and A.K. Menon. 2014. Constitutive phospholipid scramblase activity of a G protein-coupled receptor. *Nat. Commun.* 5:5115. <https://doi.org/10.1038/ncomms6115>
- Hanna, M.G., P. Suen, Y. Wu, K.M. Reinisch, and P. De Camilli. 2021. SHIP164 is a chorein motif containing lipid transport protein that controls membrane dynamics and traffic at the endosome-golgi interface. *bioRxiv*:11.04.467353. <https://doi.org/10.1101/2021.11.04.467353>
- John Peter, A.T., B. Herrmann, D. Antunes, D. Rapoport, K.S. Dimmer, and B. Kornmann. 2017. Vps13-Mcpl interact at vacuole-mitochondria interfaces and bypass ER-mitochondria contact sites. *J. Cell Biol.* 216:3219–3229. <https://doi.org/10.1083/jcb.201610055>
- John Peter, A.T., S.N.S. van Schie, N.J. Cheung, A.H. Michel, M. Peter, and B. Kornmann. 2021. Rewiring phospholipid biosynthesis reveals robustness in membrane homeostasis and uncovers lipid regulatory players. *bioRxiv*. <https://doi.org/10.1101/2021.07.20.453065>
- Jumper, J., K. Tunyasuvunakool, J. Adler, Z. Wu, T. Green, M. Zielinski, A. Zidek, A. Bridgland, A. Cowie, C. Meyer, et al. 2021. Highly accurate protein structure prediction for the human proteome. *Nature*. 596:590–596. <https://doi.org/10.1038/s41586-021s4103828-1>
- Jurrus, E., D. Engel, K. Star, K. Monson, J. Brandi, L.E. Felberg, D.H. Brookes, L. Wilson, J. Chen, K. Liles, et al. 2018. Improvements to the APBS biomolecular solvation software suite. *Protein Sci.* 27:112–128. <https://doi.org/10.1002/pro.3280>
- Kabsch, W. 2010. Integration, scaling, space-group assignment and post-refinement. *Acta Crystallogr. D Biol. Crystallogr.* 66:133–144. <https://doi.org/10.1107/S0907444909047374>
- Karatekin, E., and J.E. Rothman. 2012. Fusion of single proteoliposomes with planar, cushioned bilayers in microfluidic flow cells. *Nat. Protoc.* 7:903–920. <https://doi.org/10.1038/nprot.2012.019>
- Kocar, E., T. Lenarcic, V. Hodnik, A. Panevska, Y. Huang, G. Bajc, R. Kostanjsek, A.P. Naren, P. Macek, G. Anderluh, et al. 2021. Crystal structure of RahU, an aegerolysin protein from the human pathogen *Pseudomonas aeruginosa*, and its interaction with membrane ceramide phosphorylethanolamine. *Sci. Rep.* 11:6572. <https://doi.org/10.1038/s41598-021>
- Kumar, N., M. Leonzino, W. Hancock-Cerutti, F.A. Horenkamp, P. Li, J.A. Lees, H. Wheeler, K.M. Reinisch, and P. De Camilli. 2018. VPS13A and VPS13C are lipid transport proteins differentially localized at ER contact sites. *J. Cell Biol.* 217:3625–3639. <https://doi.org/10.1083/jcb.201807019>
- Leonzino, M., K.M. Reinisch, and P. De Camilli. 2021. Insights into VPS13 properties and function reveal a new mechanism of eukaryotic lipid transport. *Biochim. Biophys. Acta Mol. Cell Biol. Lipids*. 1866:159003. <https://doi.org/10.1016/j.bbalip.2021.159003>
- Lesage, S., V. Drouet, E. Majounie, V. Deramecourt, M. Jacoupy, A. Nicolas, F. Cormier-Dequaire, S.M. Hassoun, C. Pujol, S. Ciura, et al. 2016. Loss of VPS13C function in autosomal-recessive parkinsonism causes mitochondrial dysfunction and increases PINK1/parkin-dependent mitophagy. *Am. J. Hum. Genet.* 98:500–513. <https://doi.org/10.1016/j.ajhg.2016.01.014>
- Liebschner, D., P.V. Afonine, M.L. Baker, G. Bunkoczi, V.B. Chen, T.I. Croll, B. Hintze, L.W. Hung, S. Jain, A.J. McCoy, et al. 2019. Macromolecular structure determination using X-rays, neutrons and electrons: Recent developments in Phenix. *Acta Crystallogr. D Struct. Biol.* 75:861–877. <https://doi.org/10.1107/S2059798319011471>
- Maeda, S., H. Yamamoto, L.N. Kinch, C.M. Garza, S. Takahashi, C. Otomo, N.V. Grishin, S. Forli, N. Mizushima, and T. Otomo. 2020. Structure, lipid scrambling activity and role in autophagosome formation of ATG9A. *Nat. Struct. Mol. Biol.* 27:1194–1201. <https://doi.org/10.1038/s41594-020s4100520-2>
- Marek, M., and T. Gunther-Pomorski. 2016. Assay of flippase activity in proteoliposomes using fluorescent lipid derivatives. *Methods Mol. Biol.* 1377:181–191. [https://doi.org/10.1007/978-14939-3179-8\\_18](https://doi.org/10.1007/978-14939-3179-8_18)
- Matoba, K., T. Kotani, A. Tsutsumi, T. Tsuji, T. Mori, D. Noshiro, Y. Sugita, N. Nomura, S. Iwata, Y. Ohsumi, et al. 2020. Atg9 is a lipid scramblase that mediates autophagosomal membrane expansion. *Nat. Struct. Mol. Biol.* 27:1185–1193. <https://doi.org/10.1038/s41594-020-00518-w>
- McCoy, A.J., R.W. Grosse-Kunstleve, P.D. Adams, M.D. Winn, L.C. Storoni, and R.J. Read. 2007. Phaser crystallographic software. *J. Appl. Crystallogr.* 40:658–674. <https://doi.org/10.1107/S0021889807021206>
- Murshudov, G.N., P. Skubak, A.A. Lebedev, N.S. Pannu, R.A. Steiner, R.A. Nicholls, M.D. Winn, F. Long, and A.A. Vagin. 2011. REFMAC5 for the refinement of macromolecular crystal structures. *Acta Crystallogr. D Biol. Crystallogr.* 67:355–367. <https://doi.org/10.1107/S0907444911001314>
- Neuman, S.D., J.R. Jorgensen, A.T. Cavanagh, J.T. Smyth, J.E. Selegue, S.D. Emr, and A. Bashirullah. 2022. The Hob proteins are novel and conserved lipid-binding proteins at ER-PM contact sites. *J. Cell Sci.* 135: jcs259086. <https://doi.org/10.1242/jcs.259086>
- Park, J.S., N.M. Hollingsworth, and A.M. Neiman. 2021. Genetic dissection of Vps13 regulation in yeast using disease mutations from human orthologs. *Int. J. Mol. Sci.* 22:6200. <https://doi.org/10.3390/ijms22126200>
- Park, J.S., and A.M. Neiman. 2020. XK is a partner for VPS13A: A molecular link between chorea-acanthocytosis and McLeod syndrome. *Mol. Biol. Cell*. 31:2425–2436. <https://doi.org/10.1091/mbc.E19-08mbc.0439-T>
- Ploier, B., and A.K. Menon. 2016. A fluorescence-based assay of phospholipid scramblase activity. *J. Vis. Exp.* 54635. <https://doi.org/10.3791/54635>
- Rampoldi, L., C. Dobson-Stone, J.P. Rubio, A. Danek, R.M. Chalmers, N.W. Wood, C. Verellen, X. Ferrer, A. Malandrini, G.M. Fabrizi, et al. 2001. A

- conserved sorting-associated protein is mutant in chorea-acanthocytosis. *Nat. Genet.* 28:119–120. <https://doi.org/10.1038/88821>
- Sakuragi, T., R. Kanai, A. Tsutsumi, H. Narita, E. Onishi, K. Nishino, T. Miyazaki, T. Baba, H. Kosako, A. Nakagawa, et al. 2021. The tertiary structure of the human Xkr8-Basigin complex that scrambles phospholipids at plasma membranes. *Nat. Struct. Mol. Biol.* 28:825–834. <https://doi.org/10.1038/s41594-021-00665-8>
- Straub, M.S., C. Alvadia, M. Sawicka, and R. Dutzler. 2021. Cryo-EM structures of the caspase-activated protein XKR9 involved in apoptotic lipid scrambling. *Elife*. 10:e69800. <https://doi.org/10.7554/eLife.69800>
- Suzuki, J., E. Imanishi, and S. Nagata. 2014. Exposure of phosphatidylserine by Xk-related protein family members during apoptosis. *J. Biol. Chem.* 289:30257–30267. <https://doi.org/10.1074/jbc.M114.583419>
- Toulmay, A., F.B. Whittle, J. Yang, X. Bai, J. Diarra, S. Banerjee, T.P. Levine, A. Golden, and W.A. Prinz. 2022. Vps13-like proteins provide phosphatidylethanolamine for GPI anchor synthesis in the ER. *J. Cell Biol.* 221: e202111095. <https://doi.org/10.1083/jcb.202111095>
- Ueno, S., Y. Maruki, M. Nakamura, Y. Tomemori, K. Kamae, H. Tanabe, Y. Yamashita, S. Matsuda, S. Kaneko, and A. Sano. 2001. The gene encoding a newly discovered protein, chorein, is mutated in chorea-acanthocytosis. *Nat. Genet.* 28:121–122. <https://doi.org/10.1038/88825>
- Yanagihara, I., K. Nakahira, T. Yamane, S. Kaieda, K. Mayanagi, D. Hamada, T. Fukui, K. Ohnishi, S. Kajiyama, T. Shimizu, et al. 2010. Structure and functional characterization of *Vibrio parahaemolyticus* thermostable direct hemolysin. *J. Biol. Chem.* 285:16267–16274. <https://doi.org/10.1074/jbc.M109.074526>

## Supplemental material

Provided online are Table S1 and Table S2. Table S1 lists primers for the study. Table S2 lists data collection and refinement statistics.



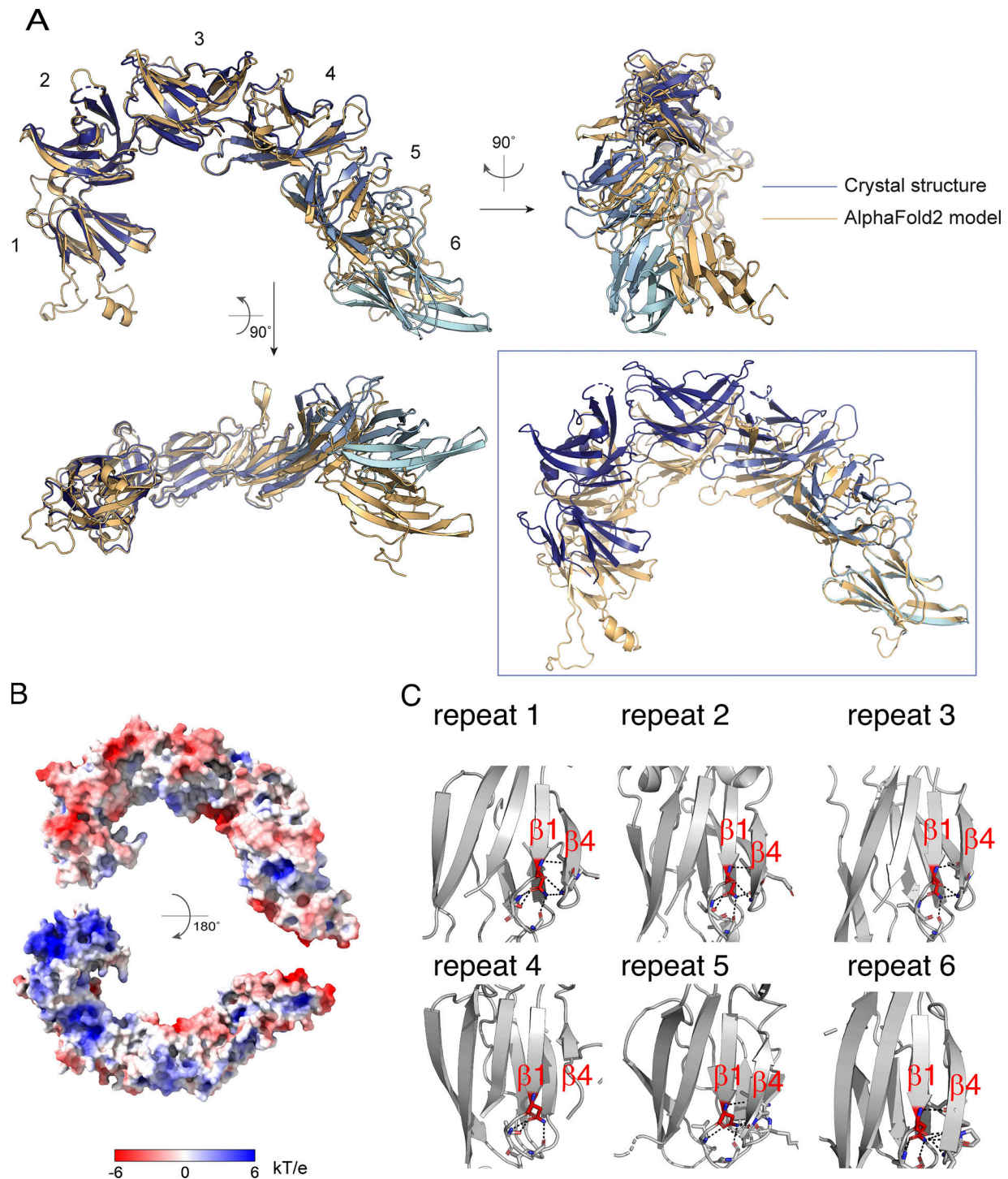


Figure S1. **Details of the VAB structure.** **(A)** Comparison of PXP-VAB<sub>1-6</sub> in the crystal structure with the prediction from AlphaFold2. AlphaFold2 accurately predicted the fold of the individual modules as well as the interfaces between modules 1 + 2 and 2 + 3. The remaining interfaces in the crystal structure differed from those in the AlphaFold2 model. At left, the structures are superimposed based on the first three modules. The positions/orientations of the remaining modules differ in the two structures. In the box, the structures are superimposed based on the sixth module only. The interface between modules 5 + 6, where the Pro-X-Pro motif binds, is different in the two models. The AlphaFold2 model does not feature the groove that is the Pro-X-Pro motif binding site. **(B)** The electrostatic potential as calculated by APBS software (Jurrus et al., 2018) mapped onto the surface of the VAB. The VAB is shown in the same orientations as in Fig. 1 C. **(C)** The asparagine at the end of  $\beta$ -strand 1, strictly conserved in all repeat modules, is involved in an extensive hydrogen bonding network that stabilizes folding of the module.